Title

Sex-specific Tau methylation patterns and synaptic transcriptional alterations are associated with neural vulnerability during chronic neuroinflammation

Authors

Didonna, Alessandro
Cantó, Ester
Shams, Hengameh
et al.

Publication Date

2019-07-01

DOI

10.1016/j.jaut.2019.04.003

Peer reviewed

HHS Public Access

Author manuscript

J Autoimmun. Author manuscript; available in PMC 2020 July 01.

Published in final edited form as:

J Autoimmun. 2019 July ; 101: 56–69. doi:10.1016/j.jaut.2019.04.003.

Sex-specific Tau methylation patterns and synaptic transcriptional alterations are associated with neural vulnerability during chronic neuroinflammation

Alessandro Didonna[1,*], **Ester Cantó**[1], **Hengameh Shams**[1], **Noriko Isobe**[1], **Chao Zhao**[1], **Stacy J. Caillier**[1], **Carlo Condello**[1,2], **Hana Yamate-Morgan**[3,4], **Seema K. Tiwari-Woodruff**[3,4,5], **Mohammad R. K. Mofrad**[6,7], **Stephen L. Hauser**[1], and **Jorge R. Oksenberg**[1]

[1]Department of Neurology and Weill Institute for Neurosciences, University of California at San Francisco, San Francisco, CA 94158, USA

[2]Institute for Neurodegenerative Diseases, University of California, San Francisco, CA 94158, USA

[3]Division of Biomedical Sciences, School of Medicine, University of California Riverside, Riverside, CA 92521, USA

[4]Neuroscience Graduate Program, University of California Riverside, Riverside, CA 92521, USA

[5]Center for Glial-Neuronal Interactions, UCR School of Medicine, CA 92506, USA

[6]Molecular Cell Biomechanics Laboratory, Departments of Bioengineering and Mechanical Engineering, University of California, Berkeley, CA 94720, USA

[7]Physical Biosciences Division, Lawrence Berkeley National Lab, Berkeley, CA 94720, USA

Abstract

The molecular events underlying the transition from initial inflammatory flares to the progressive phase of multiple sclerosis (MS) remain poorly understood. Here, we report that the microtubule-associated protein (MAP) Tau exerts a gender-specific protective function on disease progression in the MS model experimental autoimmune encephalomyelitis (EAE). A detailed investigation of the autoimmune response in Tau-deficient mice excluded a strong immunoregulatory role for Tau, suggesting that its beneficial effects are presumably exerted within the central nervous system (CNS). Spinal cord transcriptomic data show increased synaptic dysfunctions and alterations in the NF-kB activation pathway upon EAE in Tau-deficient mice as compared to wildtype animals. We

[*]**Corresponding author:** Alessandro Didonna, Department of Neurology and Weill Institute for Neurosciences, University of California San Francisco, 675 Nelson Rising Lane, San Francisco, CA 94158, USA. alessandro.didonna@ucsf.edu.

Authors' contributions

AD and JRO conceived and supervised the project. AD, EC, HS, NI, CZ and SJC carried out all the experiments. HYM and SKTW contributed research reagents. AD, EC, HS, CZ, CC, MRKM, SLH and JRO analyzed the data and wrote the paper. All authors critically reviewed and approved the final manuscript.

Competing interests

The authors declare no competing interests.

also performed the first comprehensive characterization of Tau post-translational modifications (PTMs) in the nervous system upon EAE. We report that the methylation levels of the conserved lysine residue K306 are significantly decreased in the chronic phase of the disease. By combining biochemical assays and molecular dynamics (MD) simulations, we demonstrate that methylation at K306 decreases the affinity of Tau for the microtubule network. Thus, the down-regulation of this PTM might represent a homeostatic response to enhance axonal stability against an autoimmune CNS insult. The results, altogether, position Tau as key mediator between the inflammatory processes and neurodegeneration that seems to unify many CNS diseases.

Keywords

multiple sclerosis; Tau; post-translational modifications (PTMs); neuroinflammation; lysine methylation

1. Introduction

Tau is an evolutionary conserved microtubule-associated protein (MAP) that promotes the assembly and stabilization of microtubules in neuronal axons [1]. In addition to its role in microtubule dynamics, Tau regulates adult neurogenesis, synaptic plasticity and iron export [2–4]. Tau misfolding and aggregation in the central nervous system (CNS) is the hallmark of a heterogeneous class of neurological disorders collectively known as tauopathies, which include Alzheimer's disease (AD), progressive supranuclear palsy (PSP), and fronto-temporal dementia (FTD) [5]. Initially considered as pure neurodegenerative conditions, neuroinflammatory processes have emerged as an important component of their pathophysiology, blurring the boundaries with classic autoimmune diseases of the nervous system. In fact, chronic inflammatory responses are believed to amplify initial neurotoxic insults and enhance neuronal loss through feed-forward mechanisms [6, 7].

Multiple sclerosis (MS) is a chronic CNS disorder characterized by inflammation and demyelination. MS primary etiology remains unknown but the current model of disease pathogenesis proposes the confluence and interplay between genetic and environmental factors, with over 200 genetic variants found associated with a higher risk of developing the disease [8]. Although the Tau-encoding *MAPT* was not identified as an MS susceptibility gene, progressive axonal injury and neuronal loss begin early in MS and are to a large degree refractory to available treatments. Neuro-pathology data has indeed confirmed that the pathogenic inflammation and neurodegeneration that occur in MS are overlapping and perhaps cross-dependent [9–12], suggesting the involvement of Tau in the irreversible accumulation of neurological disabilities. Consistent with this model, experimental autoimmune encephalomyelitis (EAE) –a broadly used MS animal model− in Tau-deficient mice displays a more severe disease course as compared to wildtype mice [13]. More recently, amyloid fibril-forming hexapeptides from Tau sequence have shown therapeutic effects on EAE through the activation of B-1a lymphocytes and $F4/80^{+}$ macrophages, further highlighting the cross-talk between the immune and nervous systems [14, 15].

Altogether, this body of data suggests mechanistic intersects between classic tauopathies and MS, particularly in its progressive forms. In this regard, Tau aggregates have been described

in demyelinated lesions from progressive MS patients as well as in spinal cords of mice upon chronic EAE [16, 17]. However, the molecular mechanisms by which Tau exerts its functions in autoimmune demyelination have not been elucidated yet. Post-translational modifications (PTMs) regulate the physiological functions of Tau and have been proposed to play an important role in Tau aggregation and tauopathies [18]. Thus, to fill this knowledge gap, we have applied transcriptomic and proteomic profiling in the EAE paradigm to decipher the Tau interactome and PTM profile associated with CNS autoimmunity. Here we show for the first time that methylation of the conserved K306 lysine residue in Tau affects the stability of the microtubule network within the axons. We observed that this methylation is gradually repressed at latter stages of EAE, suggesting a homeostatic response mediating the recovery from the acute EAE phase, and promoting the transition to the chronic stage of the disease.

2. Materials and Methods

2.1. Mouse strains

Mapt knockout mice (B6.129X1-Mapt^{tm1Hnd}/J) and C57BL/6J mice were purchased from The Jackson Laboratory. The generation and characterization of the Tau-null mouse line have been previously described [19]. *Mapt*$^{-/-}$ and wild type littermates (*Mapt*$^{+/+}$) were obtained from a heterozygous breeding of *Mapt*$^{+/-}$ mice. Mice were housed in a specific pathogen free (SPF) facility and all animal procedures were performed in compliance with experimental guidelines approved by the University of California, San Francisco committee on animal research (CAR).

2.2. Cell lines

HeLa cells were obtained from ATCC and maintained in Dulbecco's Modified Eagle's medium (GIBCO/Invitrogen) supplemented with 10% v/v fetal bovine serum (GIBCO/Invitrogen) and antibiotics (100 IU/mL penicillin and 100 mg/mL streptomycin) at 37°C in a humidified atmosphere with 5% CO_2.

2.3. Antibodies

The following antibodies were used in the study: TAU-5 mouse monoclonal antibody (577801, Millipore); anti-FLAG rabbit polyclonal antibody (2368, Cell Signaling); anti-α-tubulin mouse monoclonal antibody (3863, Cell Signaling); anti-β-Actin rabbit monoclonal antibody (8457, Cell Signaling); anti-rabbit IgG F(ab')2 Fragment Alexa Fluor 555 Conjugate (4413, Cell Signaling); anti-mouse IgG F(ab')2 Fragment Alexa Fluor 488 Conjugate (4408, Cell Signaling); anti-p38 MAPK (pT180/pY182) mouse monoclonal antibody (36/p38, BD Biosciences); anti-ERK1/2 (pT202/pY204) mouse monoclonal antibody (20A, BD Biosciences); anti-STAT1 (pY701) mouse monoclonal antibody (14/P-STAT1, BD Biosciences); anti-STAT3 (pY705) mouse monoclonal antibody (4/P-STAT3, BD Biosciences); anti-STAT4 (pY693) mouse monoclonal antibody (38/p-STAT4, BD Biosciences); anti-STAT5 (pY694) mouse monoclonal antibody (47/STAT5(pY694), BD Biosciences); anti-STAT6 (pY641) mouse monoclonal antibody (18/P-STAT6, BD Biosciences); anti-CD3e hamster monoclonal antibody (145–2C11, BD Biosciences); anti-CD19 rat monoclonal antibody (ID3, BD Biosciences); anti-CD4 rat monoclonal antibody

(GK1.5, BD Biosciences); anti-CD8a rat monoclonal antibody (53–6.7, BD Biosciences); anti-IL-17A rat monoclonal antibody (TC11H10, BD Biosciences); anti-IFNγ rat monoclonal antibody (XMG1.2, BD Biosciences); anti-FOXP3 rat monoclonal antibody (MF23, BD Biosciences); anti-CD44 rat monoclonal antibody (IM7, BD Biosciences); anti-CD80 armenian hamster monoclonal antibody (16–10A1, BioLegend).

2.4. DNA constructs

The pcDNA3.1 vector containing the full-length coding sequence of human *MAPT* (2N4R) with a FLAG epitope at the C-terminus was used to express wildtype Tau in cell lines. Construct expressing the Tau mutants K317A, K317Q and K317R were generated by introducing missense point mutations in the *MAPT* sequence with the QuickChange Lightning Site-Directed Mutagenesis Kit (Stratagene). The following primers were used: K317R forward, 5′-CCAGTTGACCTGAGCAGGGTGACCTCCAAGT-3′; K317R reverse, 5′-ACTTGGAGGTCACCCTGCTCAGGTCAACTGG-3′; K317A forward, 5′-AACCAGTTGACCTGAGCGCGGTGACCTCCAAGTGTG-3′; K317A reverse, 5′-CACACTTGGAGGTCACCGCGCTCAGGTCAACTGGTT-3′; K317Q forward, 5’-CCAGTTGACCTGAGCCAGGTGACCTCCAAGT-3’; K317Q reverse, 5’-ACTTGGAGGTCACCTGGCTCAGGTCAACTGG-3’. Individual clones were confirmed by Sanger sequencing.

2.5. EAE induction

Active EAE was induced following previously published procedures [20]. Briefly, 8–10 week old mice were injected subcutaneously with 100 μg of $MOG_{35–55}$ peptide (EZBiolab), in complete Freund’s adjuvant (CFA) with 4 mg/mL *Mycobacterium tuberculosis* (DIFCO Laboratories). Mice also received 400 ng of pertussis toxin (LIST Biological Laboratories) intraperitoneally both immediately after immunization and 48 hours later. Control mice were injected with everything except the MOG peptide. For all experiments animals were observed daily, and clinical signs were assessed as follows: 0, no signs; 1, decreased tail tone; 2, mild monoparesis or paraparesis; 3, severe paraparesis; 4, paraplegia; 5, quadriparesis; and 6, moribund or death. All scores were assigned blindly to the genotypes of the mice. All animal experiments were conducted according to protocols approved by the local animal welfare committee.

2.6. Cuprizone demyelination induction

Chronic demyelination was induced by feeding 10 week old C57BL/6J male mice ad libitum 0.2% w/w cuprizone (biscyclohexane oxaldihydrazone, Sigma) milled into mouse chow for a period of 12 weeks. Age- and sex-matched mice on regular chow were used as non-treated controls. The region of the corpus callosum (CC) was dissected for downstream analysis from both treated and non-treated mice, following previously published procedures [21]. Briefly, brains were dissected and placed into an Adult Mouse Brain Slicer Matrix (BSMAS005–1, ZIVIC Instruments) where 2.5 mm thick coronal slabs were cut. The portion containing the CC was then quickly excised from each slab and snap frozen on dry ice.

2.7. Histopathology

Mice were perfused with 4% paraformaldehyde (PFA) in phosphate buffered saline (PBS). Spinal cords were dissected and post-fixed in 4% PFA for additional 48 hours before processing for paraffin embedding. Transversal sections of 5 μm were then cut and stained with Hematoxylin and Eosin (H&E) or Luxol Fast Blue (LFB) in order to measure lymphocyte infiltration and demyelination. Semi-quantitative analyses were carried out blindly to the genotype on 3 sections from representative anatomical regions of the spinal cord (cervical, thoracic and lumbar) by counting the number of inflammation foci (defined as groups of at least 20 infiltrating cells) and demyelinated areas. Demyelination was assessed independently on both H&E and LFB stained sections and the relative scores were combined. The mean of the three values was then calculated and average inflammation and demyelination scores were assigned to each mouse. Both tissue processing and histopathological analysis were outsourced at Hooke Laboratories (Lawrence, MA).

2.8. Western blot assays

Spinal cords were dissected and homogenized in 10 volumes of cold RIPA buffer (Tris-HCl pH 7.5, 50 mM; NaCl, 150 mM; NP-40, 1%; sodium deoxycholate, 0.5%; SDS 0.2%) supplemented with complete protease inhibitors (Roche). Homogenates were then incubated on ice for 30 min and spun for 10 min at 16000×g to remove cell debris. Supernatants were collected and total proteins were quantified using the Bicinchoninic (BCA) Protein Assay Kit (Pierce). About 40 μg of total proteins were separated by SDS-PAGE on 10% polyacrylamide gels and then blotted onto nitrocellulose membranes (Immobilion) at 100V for 30 min. Membranes were subsequently blocked with 5% milk in Tris buffered saline with 0.05% Tween-20 (TBS-T) for 1 hour at room temperature (RT). After blocking, membranes were incubated with primary antibodies diluted (1:1000) in blocking solution or 5% bovine serum albumin (BSA) in TBS-T overnight at 4°C. The day after, the membranes were washed 3 times with TBS-T and incubated with horseradish peroxidase (HRP)-conjugated IgG (Cell Signal Technology) in blocking solution (1:5000) for 1 hour at RT. After extensive washing, membranes were incubated with Supersignal West Dura reagent (Thermo Scientific) and the chemiluminescent signals were detected using a Molecular Imager ChemiDoc XRS System equipped with Quantity One software (Bio-Rad).

2.9. Tau immunoprecipitation

Total Tau was isolated from spinal cord or CC lysates using the Crosslink Immunoprecipitation Kit (Pierce). Tissues were homogenized in 10 volumes of cold Thermo IP Lysis Buffer supplemented with 3 μM trichostatin A (pyridine-3-carboxylic acid amide, Sigma), 10 mM niacinamide (Sigma) and Halt Protease and Phosphatase Inhibitor Cocktail (Fisher). Lysates were then sonicated on ice twice for 5 minutes with a sonicator at 40% amplitude and spun at 10,000×g for 10 minutes at 4 °C. Supernatants were collected and protein concentration was measured using the Bicinchoninic (BCA) Protein Assay Kit (Pierce). Lysate volumes containing 1 mg of total proteins were first pre-cleared with 40 μL of Control Agarose Resin for 1 hour at 4° C and then were incubated with 30 μg of TAU-5 mAb crosslinked to Protein A/G Plus Agarose beads for 10 hours at 4 °C, rotating. Beads were washed 4 times with IP lysis buffer and once with TBS before eluting the bound

proteins with 50 μL of Pierce Elution Buffer. For in-solution trypsin digestion before mass spectrometry, immunoprecipitated samples were neutralized with 1 M Tris, pH 9.6, supplemented with 3 μM trichostatin A, 10 mM niacinamide and Halt Phosphatase Inhibitor Cocktail (Fisher).

2.10. Mass spectrometry analysis

Proteins were crashed using −80 °C acetone and stored overnight at −80 °C. Samples were then mildly vortexed followed by centrifugation at 10,000×g for 10 minutes, at 4 °C. The supernatants were discarded and the protein pellets were allowed to air dry under a fume hood for 20 minutes. The protein pellets were subsequently resuspended in 0.2% Protease Max (Promega) 50 mM ammonium bicarbonate and the proteins were reduced with 10 mM dithiothreitol (DTT) at 55 °C for 30 minutes. Samples were allowed to come to room temperature followed by alkylation using 30 mM propionamide at room temperature for 30 minutes. Proteins were then digested using Trypsin/LysC (Promega) at a protein to protease ratio of 100:1, respectively. Samples were digested overnight at 37 °C followed by quenching with addition of formic acid to 0.5% (v/v). The peptides were purified using C18 monospin columns (GL Sciences) and quantified by a fluorometeric assay (Pierce). Eluted peptides from each sample were injected onto an in-house pulled and packed analytical column (C18, Dr. Maisch 2.4 μm) where the UPLC was a Waters nanoAcquity or M-Class. In a typical experiment the flow rate was 450 nL/min with a linear gradient where mobile phase A was 0.2% formic acid, 99.8% water and mobile phase B was 0.2% formic acid, 99.8% water. The mass spectrometer was either an Orbitrap Fusion or Orbitrap Elite, operated in data dependent acquisition mode (DDA) to fragment the 15 most intense multiply charged precursor ions. In a typical analysis, .raw files were processed using Byonic v2.10.5 (Protein Metrics, San Carlos, CA). These analyses assumed fully tryptic digestion, and allowed for up to 2 missed cleavages. Precursor ion mass tolerances were set to 12 ppm, with 0.4 Da mass tolerances for CID fragment ions. Data were searched against the Uniprot *Mus musculus* proteome updated 20161025 including isoforms, and concatenated with a list of common background contaminant proteins prior to analysis. All data were cut at a 1% false discovery rate using the reverse decoy strategy [22]. Following analysis, MatLab and Excel scripts were used to prepare the data.

2.11. RNA isolation and RNA-seq

Total RNA was extracted from spinal cords using the Trizol reagent (Invitrogen) and cleaned up with the RNeasy Mini Kit (Invitrogen). DNA contaminations were removed by on-column digestion using the RNase-free DNase Set (Qiagen). The quality of RNA was confirmed with the BioAnalyzer 2100 (Agilent) and all samples showed RIN values between 8.2 and 9.6. Next Generation Sequencing was performed on a GAIIx platform (Illumina) following the stranded Truseq protocol and generating 40 million of paired-end 50 bp reads per sample. After initial QC, the reads were aligned to the most recent mouse genome reference (mm10) and assembled into transcripts using the STAR aligner [23]. A logistic regression model (EA Ensemble method) was then employed to estimate the differentially expressed genes between genotypes. P values of 0.05 or less after false discovery rate (FDR) correction were considered significant. All sequencing steps as well as data analyses were performed by Expression Analysis, Inc (Durham, NC).

2.12. Quantitative RT-PCR analysis

For mRNA analysis, 1μg of total RNA was retro-transcribed into cDNA with the SuperScript III First-Strand kit (Invitrogen), and 0.5 μL of the total reaction volume was used for quantitative RT-PCR. All amplifications were performed on a Mx3005P thermocycler (Stratagene), using the Power SYBR Green PCR Master Mix (Applied Biosystems). Gene expression levels were analyzed using the following primers: SNCA forward, 5′-GGGAGTCCTCTATGTAGGTTCC-3′; SNCA reverse, 5′-TCCAACATTTGTCACTTGCTCT-3′; DNM1L forward, 5′-TTACGGTTCCCTAAACTTCACG-3′; DNM1L reverse, 5′-GTCACGGGCAACCTTTTACGA-3′; STXBP1 forward, 5′-GTGGACCAGTTAAGCATGAGG-3′; STXBP1 reverse, 5′-GCTCTCGGCGCTTGTTGAT-3′; MAP3K14 forward, 5’-TGTGGGAAGTGGGAGATCCTA-3’; MAP3K14 reverse, 5’-GGCTGAACTCTTGGCTATTCTCA-3’; IKBKE forward, 5’-ACCACTAACTACCTGTGGCAT-3’; IKBKE reverse, 5’-CCTCCCCGGATTTCTTGTTTC-3’; RIPK3 forward, 5’-TCTGTCAAGTTATGGCCTACTGG-3’; RIPK3 reverse, 5’-GGAACACGACTCCGAACCC-3’; GAPDH forward, 5’-CATGGCCTTCCGTGTTCCTA-3’; GAPDH reverse, 5’-CCTGCTTCACCACCTTCTTGAT-3’. Each sample was run in triplicate and the $\Delta\Delta C_t$ method was used for relative quantification, with *Gapdh* expression levels serving as internal control.

2.13. T cell proliferation assay

Splenocytes were isolated from *Mapt*$^{-/-}$ and wildtype male mice after 11 days from immunization with 100 μg of $MOG_{35–55}$ peptide in CFA. Cells were cultured in 96-well microtiter plates at a concentration of 10^6 cells/mL in the presence of crescent concentrations of $MOG_{35–55}$ peptide. Culture medium consisted of RPMI 1640 (GIBCO/Invitrogen) supplemented with 2 mM l-glutamine, 1 mM sodium pyruvate, 50 μM 2-mercaptoethanol, 10% (vol/vol) fetal bovine serum and antibiotics (100 IU/mL penicillin and 100 mg/mL streptomycin). Cells were cultured for 72 hours and pulsed for the last 18 hours with 1 μCi/well [^{3}H]-thymidine before harvesting. Radioactive signals were measured with a 1450 Microbeta Trilux liquid scintillation counter (PerkinElmer).

2.14. Lymphocyte activation assay

Cell activation was assessed by measuring the surface expression of the activation markers CD44 and CD80 by flow cytometry. Briefly, splenocytes from MOG peptide-primed mice were cultured for 72 hours in 24-well plates at a concentration of 10^6 cells/mL in complete RPMI 1640 medium in the presence of 5 or 25 μg/mL of $MOG_{35–55}$ peptide. Then, cells in suspension were collected and the adherent cells were detached with PBS-0.05% EDTA on ice for 30 minutes. Cells were then washed with PBS, blocked with Fc blocking reagent (Miltenyi Biotech) following the manufacturer’s protocol, and subsequently stained with cell-specific marker antibodies as well as anti-CD44 and anti-CD80 antibodies.

2.15. Th1, Th17 and Treg differentiation

Splenocytes were isolated from *Mapt*$^{-/-}$ and wildtype male mice after 11 days from immunization with 100 μg of $MOG_{35–55}$ peptide in CFA. Cells were cultured in 24-well plates at a concentration of 10^6 cells/mL in complete RPMI 1640 medium in the presence of 10 μg/mL of $MOG_{35–55}$ peptide. Polarization towards the different lineages was promoted with 20 ng/mL IL-23 and 20 ng/mL IL-6 (for Th17), 10 ng/ml IL-12 (for Th1) or 5 ng/mL TGF-β1 (for Treg). After 72 hours, the percentage of $CD4^+$ T cells differentiated to each cell lineage was quantified by flow cytometry using a LSRFortessa instrument equipped with FACSDiva software (BD Biosciences). Briefly, Th1 and Th17 cells were assessed by intracellular cytokine staining of IFN-γ and IL-17 using the Fixation and Permeabilization Solution Kit (BD Biosciences) after activating the cells for 4 hours with the Cell Activation Cocktail (Fisher) in the presence of Protein Transport Inhibitor Cocktail (Fisher). Treg cell differentiation was instead assessed by FOXP3 staining using the FoxP3 Buffer Set (BD Biosciences).

2.16. Phosphoflow cytometry

We have optimized a robust protocol to simultaneously determine by flow cytometry the levels of 7 key signaling phosphoproteins [P38 mitogen-activated protein kinase (p38MAPK), Extracellular Signal-regulated Kinase 1/2 (ERK1/2) and Signal Transducers and Activators of Transcription 1, 3, 4, 5, 6 (STAT1, STAT3, STAT4, STAT5, STAT6)] in 3 relevant immune cell subsets ($CD4^+$ and $CD8^+$ T cells, and B cells) [24]. Briefly, splenocytes were isolated from Mapt$^{-/-}$ and wildtype male mice after 11 days from immunization with 100 μg of $MOG_{35–55}$ peptide in CFA. The cells were then re-stimulated in culture with 10 μg/mL of $MOG_{35–55}$ peptide for 24 hours. Then, the splenocytes were fixed with 1.5% PFA and permeabilized with 100% ice-cold methanol for 30 minutes on ice. After washing, cells were stained with fluorophore-conjugated antibodies specific for the different phosphoproteins and cell markers, and analyzed using a LSRFortessa instrument equipped with FACSDiva software (BD Biosciences). To generate heatmaps, the mean fluorescence intensity (MFI) values for each phosphorylated protein in each cell type were transformed into Z-scores and plotted according to the following color code: proteins displaying positive values in the levels of phosphorylation are depicted in red while proteins shown negative values are depicted in blue. Proteins showing no changes in their phosphorylation state are instead represented in white.

2.17. Microtubule binding assay

To study the interaction between tau and microtubules we adapted a previously published protocol [25]. Briefly, HeLa cells were cultured in 60 mm plates and transfected at 90% confluence with 5 μg of the different *MAPT* constructs using Lipofectamine 2000 (Invitrogen), according to manufacturer's instructions. After 24 hours, cells were washed twice with warm PBS and lysed in 500 μL of warm 80 mM PIPES buffer pH 6.8, 1mM guanosine-5'-triphosphate, 1 mM $MgCl_2$, 1 mM EGTA, 0.5% w/v Triton X-100 and 30% v/v glycerol, supplemented with 1 mM phenylmethylsulfonylfluoride, complete protease inhibitors (Roche), 0.5 μM okadaic acid (Calbiochem), and 10 μM taxol (Sigma). Cell lysates were spun at 5000×g for 5 minutes at room temperature (RT) to pellet the nuclei.

Clarified lysates were then centrifuged at 100,000×g for 1 hour at RT using an Optima ultracentrifuge (Beckman). The supernatants were retained as the microtubule unbound fraction while the pellets were washed once with PIPES buffer and resuspended in 150 μL of 2X Laemmli buffer (microtubule bound fraction). Equal volumes of both bound and unbound fractions were probed by Western blot using an anti-FLAG antibody. The relative affinity of each Tau mutant for microtubules was then expressed as the ratio between the signal intensity of the bound over the unbound fraction.

2.18. Microtubule bundling assay

HeLa cells were cultured in 24 well plates and transfected at 90% confluence with 0.5 μg of the different *MAPT* constructs using Lipofectamine 2000 (Invitrogen), according to manufacturer's instructions. After 24 hours, cells were reseeded onto poly-L-lysine (Sigma) coated glass coverslips and let grow ON. The day after, cells were fixed with 4% PFA in PBS for 20 min at 37 °C. After 3 washes in PBS, cells were permeabilized with 0.3% Triton XT-100 in PBS for 5 min and then blocked with 5% normal goat serum (NGS, Cell Signaling) in PBS supplemented with 0.1% Triton XT-100 (PBS-T) for 1 hour at RT. Cells were washed once and subsequently incubated with anti-FLAG (1:200) and anti-tubulin (1:600) antibodies in 1% bovine serum albumin (BSA) in PBS-T ON at 4 °C. After 24h, cells were washed 3 times with PBS-T and incubated with anti-mouse and anti-rabbit secondary antibodies conjugated with Alexa Fluor 488 or 555 (1:1000) in 1% BSA for 1 hour at RT. After 3 more washes, the coverslips were mounted onto glass slides using Vectashield with DAPI (Vector Laboratories). Cells were imaged (40X magnification) using an Eclispe Ti-E microscope equipped with NIS-Elements software (Nikon). Within each experiment, 5–6 random fields were imaged for each construct and analyzed using ImageJ software (https://imagej.nih.gov). Microtubule bundling propensity was expressed as the percentage of transfected cells exhibiting microtubule bundles.

2.19. Protein stability assay

HeLa cells were cultured in 60 mm plates and transfected at 90% confluence with 5 μg of the different *MAPT* constructs using Lipofectamine 2000 (Invitrogen), according to manufacturer's instructions. After 24 hours, cells were treated with 25 μg/mL cycloheximide (CHX, Sigma) for 6, 12 and 24 hours. At the different time points, cells were washed twice with cold PBS and lysed in 250 μL of RIPA buffer supplemented with protease inhibitors. Untreated transfected cells were also collected as baseline. Cell lysates were spun at 5000×g for 5 minutes and supernatants were retained for subsequent analysis. Protein concentration was assessed and volumes equal to 10 μg of total proteins were probed by Western blot for Tau levels using an anti-FLAG antibody. Actin levels were used as internal controls. The stability of each Tau mutant was then expressed as the percentage of normalized Tau levels at the different time points analyzed, as compared to the levels of the same mutant at baseline.

2.20. Molecular dynamics simulations

The structure of human Tau fragment including residue K317 was obtained from isolating one chain from amyloid filaments extracted from AD brain (PDB ID: 5O3T) [26]. The Tau fragment was solvated and C_α atoms were constrained, while side chains were moved to

reduce bad contacts. The tubulin dimer was taken from a longer chain with 1.8 Å resolution and equilibrated in a water box (PDB ID: 5IYZ) [27]. The Tau fragment was then positioned between tubulin monomers such that K311 on Tau faced residues K336 and K338 of α-tubulin [28]. The Tau-tubulin complex was solvated and ionized at a final KCl concentration of 150 mM. The K317R mutation was modeled using Visual Molecular Dynamics (VMD) Mutation Plugin [29]. Methylation was modeled by adding the methyl group to the nitrogen atom at the end of the K317 sidechain. The parameters of mono-methylated lysine were implemented from [30].

The complex was minimized for 500,000 steps and equilibrated using NAMD molecular dynamics package and CHARMM force field [31, 32]. Simulations were performed using an NPT ensemble in which the temperature was kept constant at 310° K using the Nose-Hoover thermostat, and pressure was maintained at 1 atm using the Langevin piston [33]. A time-step of 2 fs was used in all simulations. The Particle Mesh Ewald Method was employed for long-range electrostatic interactions. The van der Waals (VDW) interactions were smoothly reduced at the 1.2 nm cutoff distance via switching function. The production simulation was performed for 1μs. All visualizations and post-processing were carried out with VMD and in-house scripts in R. Binding pocket volumes were measured using POVME[34] and molecular volumes were calculated by VDW radii. All MD simulations were conducted in a computer cluster of the Extreme Science and Engineering Discovery Environment (XSEDE) at the University of Tennessee [35].

2.21. Bioinformatic analyses

The differentially expressed genes (DEGs) identified by RNA-seq were mapped onto a high-quality curated protein–protein interaction network accessible at the Human Protein Reference Database (HPRD; http://www.hprd.org) [36]. The local Tau network was subsequently generated with the Cytoscape software [37] by extracting the Tau neighbor DEGs up to the third degree of connectivity. The molecular function and biological process ontologies associated to the Tau local network were then annotated using the Enrichment Analysis tool of the Gene Ontology Consortium (http://www.geneontology.org) [38]. Enriched terms in each gene ontology (GO) category were searched against the whole mouse transcriptome and Bonferroni post-hoc test was used for multiple-test correction, considering significant P values of 0.05 or less. To reduce the redundancy of GO analysis, we reported only the significant GO terms at the top of each GO hierarchy.

2.22. Statistical analyses

Differences between means of two groups were assessed with Mann-Whitney U test or Student’s t-test as indicated. P values equal to 0.05 or less were considered significant. Data were expressed as mean ±SEM. For proteomic analysis, the relative site occupancy for each PTM was calculated as the ratio between the number of detected peptides containing the modified amino acid and the total number of peptides containing that amino acid (modified and unmodified). The differences in the PTM site occupancy between EAE mice and mock immunized controls were compared by one-way ANOVA. In multiple comparisons, P values were corrected by false discovery rate (FDR) for each type of modification. As an additional quality control, only the PTMs that were consistently detected in all the biological replicates

were included in the analysis. The patterns of PTM changes over time between two groups were determined by linear mixed-effects regression models with subject-level repeated observations at different time points, which were taken into account as random effects. The P value of interaction term (Group * Time) was used to determine both group and time effects on PTMs. The standard level of significance used to justify a claim of a statistically significant effect is 0.05 or less. All analyses were performed in R 3.4.2. The linear mixed-effects models were performed with the R package nlme.

3. Results

3.1. EAE is exacerbated in Tau-null mice

In order to study the role of Tau in autoimmune demyelination, we studied in detail the effects of Tau ablation on EAE, a murine induced disease that recapitulates several features of MS, including CNS infiltration of autoreactive lymphocytes, demyelination, and axonal transection [39–41]. Tau-null mice are viable and do not show any overt phenotype, excluding subtle cognitive defects in aged animals [42]. We hence immunized both *Mapt*$^{-/-}$ and *Mapt*$^{+/+}$ 8–10 week old mice with myelin oligodendrocyte glycoprotein peptide 35–55 ($MOG_{35–55}$) (Fig. S1). As previously reported [13], the EAE course was more severe in knockout mice as compared to wildtype littermate controls, with no differences in disease onset (Fig. 1A). However, these differences were observed exclusively in males as no significant changes in disease scores or in the onset were observed in female knockout animals (Fig. 1B).

We next asked whether the differences in the EAE phenotype in male Tau-null mice were caused by increased CNS inflammation or by more severe CNS degeneration. To address this question, we performed histopathological analysis on spinal cords collected at 31 dpi, when the divergence in EAE profiles between knockout and wildtype animals was maximum. No difference was observed in the number of lymphocyte foci infiltrating the CNS parenchyma (Fig. 1C), while a significant increase in myelin loss was found in spinal cords of knockout animals (Fig. 1D). These findings are consistent with the previous report of more extended axonal damage in the white matter of Tau-deficient mice upon EAE, without significant differences in the number of inflammatory cells [13].

We also analyzed the histopathology of female mice at the same EAE time point (Fig. S2A–B). No statistically significant differences in demyelination levels were observed between wildtype and knockout mice, paralleling their clinical scores. Interestingly, a higher number of infiltrating cells was found in Tau-deficient females.

3.2. Tau ablation does not affect peripheral immune responses

The histopathology results suggest that the modifier role for Tau in autoimmune demyelination is independent from the magnitude of the CNS inflammatory infiltrate. To further explore this premise, we carried out a thorough characterization of the immune response in Tau-null male mice to assess any possible contribution to the EAE phenotype of Tau ablation in the immune system, especially considering that *Mapt* is expressed in lineages relevant to autoimmunity such as Th17 and Treg cells [43].

First, we tested if Tau ablation in lymphocytes affects their proliferation capacity in response to the encephalitogenic MOG peptide. No significant differences were detected between splenocytes from *Mapt*$^{-/-}$ and wildtype mice (Fig. 2A). We then analyzed the capacity of CD4^{+} T cells to polarize toward pro-inflammatory (Th1/Th17) or tolerogenic (Treg) lineages *in vitro* (Fig. 2B; Fig. S3). Also in this case, we did not find any significant difference in the percentage of CD4^{+} T cells polarized to the different cell phenotypes between Tau-null and wildtype cells. Likewise, the surface expression levels of two well-established activation markers (CD44 and CD80) were similar in both genotypes, with the only exception of elevated CD80 expression in wildtype CD4^{+} T cells (P=0.03) (Fig. 2C). Lastly, we employed phosphoflow cytometry to profile the activation status of seven key signaling proteins (p38, ERK1/2, STAT1, STAT3–6) in response to MOG peptide stimulation. The levels of phosphorylated STAT1 and STAT6 were found moderately higher in both wildtype CD4^{+} T cells (P_{STAT1}=0.04; P_{STAT6}=0.03) and CD8^{+}T cells (P_{STAT1}=0.03; P_{STAT6}=0.03) as compared to knockout cells. STAT3 was instead found more activated in wildtype B cells (P=0.05) (Fig. 2D). Collectively, this data suggest that the exacerbated EAE phenotype observed in Tau-null mice cannot be fully explained by substantial alterations in the adaptive peripheral immune cellular compartment. In light of these results, we subsequently focused our investigation on Tau function in the nervous system during EAE.

3.3. Specific neuronal pathways are dysregulated in Tau-null mice

A detailed transcriptomic profiling of CNS from Tau-null and wildtype male mice upon EAE was carried out using RNA-seq technology. Given the fact that *Mapt* is expressed in both neuronal and glial cells [44], we used total RNA from whole spinal cord tissues. Comparative analysis identified 3,421 differentially expressed genes (DEGs) between knockout and wildtype animals (1,498 up-regulated and 1,923 down-regulated), reflecting substantial systemic alterations in the CNS transcriptional landscape resulting from the absence of Tau (Table S1). These differences are sufficient to clearly segregate knockout and wildtype genetic profiles using unsupervised hierarchical clustering (Fig. 3A). A number of cellular functions are associated with these genes (Table S2), including “microtubule binding” (fold increase: 1.98, $P_{corr}=8.22\times10^{-3}$), as expected. In order to isolate the core of processes directly affected by Tau ablation, we mapped the differentially expressed genes onto the Tau interactome extracted from a curated database of experimentally validated protein interactions (Human Protein Reference Database, HPRD), hence defining a Tau-centered subnetwork of 41 nodes (Fig. 3B). GO analysis (Table S3) identified the category “positive regulation of neurotransmitter secretion” as the most enriched biological process in the network (fold increase: 150, $P_{corr}=1.84\times10^{-2}$), mainly driven by the downregulation of α-synuclein (*Snca*), dynamin 1-like (*Dnm1l*), and syntaxin-binding protein 1 (*Stxbp1*) genes (Fig. 3C). On the other hand, the up-regulation of genes encoding for receptor interacting serine/threonine kinase 3 (*Ripk3*), inhibitor of nuclear factor kappa-B kinase subunit epsilon (*Ikbke*), and mitogen-activated protein kinase kinase kinase 14 (*Map3k14*) is connected to the strong enrichment of the molecular function category “NF-κB-inducing kinase activity” in the network (fold increase: 300, $P_{corr}=6.67\times10^{-4}$) (Fig. 3D). Quantitative PCR (qRT-PCR) assays independently validated the results of RNA-seq analysis for the differential expression of *Snca*, *Stxbp1*, *Ripk3*, *Ikbke* and *Map3k14* genes, but not for *Dnm1l* (Fig. 3E). Notably, the expression of these genes is not altered in naïve *Mapt*$^{-/-}$ male mice (Fig. 3F),

suggesting that the pathways to which they belong are dysregulated specifically in response to an encephalitogenic challenge and not in steady-state conditions.

To further explore the molecular basis of the sex-related differences in the EAE phenotype, we also carried out RNA-seq on the CNS isolated from Tau-null and wildtype female mice at the same EAE time point. We then performed pairwise comparisons between either genotypes or genders. Remarkably, no DEGs were found between wildtype and knockout EAE females, consistent with the lack of differences in their EAE course. On the contrary, 2,257 DEGs were identified between wildtype EAE males and females (Table S1). GO analysis on these genes resulted in a number of molecular processes differentially regulated between sexes in response to the encephalitogenic challenge (Table S2). Among them, we found a significant enrichment in the "regulation of cytoskeleton organization" (fold increase: 2, $P_{corr}=2.62\times10^{-5}$). This molecular function seems related to the differential expression of 59 genes involved in "tubulin binding" (fold increase: 1.95, $P_{corr}=0.03$), with *Snca* being the most upregulated gene in males as compared to females. Lastly, 99 DEGs were found between Tau-null females and males, but no significant GO terms were found associated to them (Table S1).

3.4. Tau is differentially methylated in the CNS upon EAE

The transcriptomic profiling described above suggests that Tau might regulate the sensitivity of neurons toward inflammatory insults. In order to mechanistically understand how Tau mediates this function, we decided to describe its EAE-associated PTM code as Tau activity is strictly dependent on the complex set of PTMs. Our rationale for using EAE (i.e. experimental) tissue derives mainly from the possibility to better preserve PTMs and perform longitudinal studies along disease progression. Moreover, similar to MS, permanent neurological disability in EAE is also determined by axonal loss [45].

We induced EAE in *Mapt*$^{+/+}$ C57BL/6J male mice and harvested spinal cords at key stages of the disease: baseline (0 dpi), disease peak (20 dpi), recovery phase (40 dpi) and chronic phase (78 dpi). Spinal cord tissues from mock immunized animals (adjuvant and pertussis toxin) were also collected at the same time points as controls (Fig. 4A). Total Tau was then immunoprecipitated from whole spinal cord lysates using the TAU-5 mAb and processed for mass spectrometry PTM discovery. After applying a stringent analysis pipeline, we compared the relative site occupancy frequencies for the PTMs that passed our inclusion criteria between EAE and mock samples at each time point (Table S4). Remarkably, only one PTM, the mono-methylation of lysine residue 306 (metK306), showed a significant difference in frequency, being present more in controls (mock) than in EAE samples (Fig. 4B), and reaching statistical significance at 40 dpi ($P_{corr}=0.05$) and 78 dpi ($P_{corr}=0.004$). This trend is consistent with the hypothesis that the methylation of K306 is differentially regulated along EAE progression. Hence, we built a linear regression model to analyze its variation in function of time within each dataset (from baseline to 78 dpi) and confirmed that the longitudinal profiles of metK306 frequency in EAE and controls are significantly different ($P=0.001$).

In a separate set of experiments, we tested for metK306 levels in total Tau immunoprecipitated from the spinal cords of C57BL/6J female mice at similar EAE stages

(baseline, 20 dpi and 90 dpi). Notably, we did not detect any methylation at K306 either in female EAE or in controls, at all the selected time points.

Lastly, we tested whether this difference is specific of autoimmune demyelination or it is the result of any degenerative process taking place in the CNS. To address this question, we took advantage of the cuprizone paradigm, a neurotoxic MS model in which CNS demyelination is chemically induced in the absence of infiltrating encephalitogenic lymphocytes [46]. C57BL/6J male mice were fed 0.2% cuprizone chow for 12 weeks to induce chronic demyelinated lesions in the corpus callosum region, which was dissected and subjected to proteomic PTM profiling. No statistically significant differences were measured for any of the PTMs identified in this white matter structure in comparison to animals fed with standard diet (Table S5).

3.5. Methylation at K306/K317 diminishes microtubule binding

The K306 residue in mouse Tau is located within the R3 microtubule-binding domain and it is evolutionary conserved, corresponding to K317 in the human sequence. Given its critical position for Tau function, we decided to explore the molecular implications of this PTM and assess whether the addition of a methyl group to K306/ K317 is able to alter Tau interaction with microtubules. We generated a tau mutant in which the K317 residue in the longest human sequence (2N4R) was replaced with an arginine (K317R), mimicking the methylation of the lysine residue by increasing both the local bulkiness and hydrophobicity of the distal R group [47]. We generated two additional mutants by introducing the smaller alanine (K317A) to produce a maximal change in the local structure, and a glutamine (K317Q) as a mimic for acetylated lysine, another PTM observed at K306 [48, 49]. Each construct was then transfected into HeLa cells and the affinities of the different Tau mutants for microtubules were measured as the ratios between the microtubule-bound and the unbound fractions, isolated by ultra-centrifugation (Fig. 4C). All the three Tau methyl-mimics show a decrease in their ability to interact with microtubules–K317R and K317Q displaying a reduction of 60% and K317A of 40% as compared to wildtype Tau. Notably, such differences in binding cannot be ascribed to impaired protein stability as confirmed by time-course cycloheximide (CHX) experiments (Fig. 4D).

To assess the effects of the differential binding on microtubule dynamics, we then measured the ability of each Tau mutant to induce the formation of stable microtubule bundles in cells [50]. After 48 hours from transfection, 30% of Hela cells expressing wildtype Tau exhibited bundles of microtubules in their cytosol. In contrast, all mutants showed significantly less cells with bundles, ranging from 25% of positive cells for K317R and K317Q to 21% for K317A (Figs. 4E–4G). These findings are consistent with our previous biochemical analysis and confirm that PTMs at K306/K317 diminish the stabilizing activity of Tau on the microtubule network.

3.6. Effects of K317 methylation on the Tau–microtubule interaction characterized by molecular simulations

Although arginine is widely used as a *bona fide* proxy for methylated lysine, this amino acid does not recapitulate all the structural features of this PTM. Moreover, very little data exists

on the implication of lysine methylation for Tau function. For these reasons, we decided to further validate our methyl-mimic approach by employing molecular dynamics (MD) simulations, using recently reported high resolution structures of Tau to model the effects of PTMs on protein function at the atomic level [26]. For this set of experiments, we used the structure of the Tau segment between 306–378 residues of human 2N4R Tau (PDB ID: 5O3T), and compared both K317 methylation and K317R substitution for their effects on microtubule binding. As proposed by the work of Kadavath et al. [28], residue 311 of Tau was initially positioned next to residues 336 and 338 of α-tubulin (Fig. 5A). The methylated and mutated structures of Tau were superimposed on the wildtype one resulting in similar starting configurations of all three structures, allowing for a direct comparison between their microtubule-binding capabilities.

We first measured the interaction energies between the different forms of Tau and tubulin. Remarkably, we found that both methylation at K317 and arginine substitution result in significantly lower binding strength ($P<2.2\times10^{-16}$) toward tubulin heterodimer as compared to the non-methylated state (Fig. 5B). When the affinity for single tubulin monomers was tested, non-methylated Tau remained at the binding interface of the tubulin heterodimer, whereas both methylated and mutated Tau partially detached from the interface and shifted towards one monomer (Fig. 5B; Movie S1). Altogether, these results are in agreement with our experimental data and confirm the validity of arginine mutation for mimicking lysine methylation in biochemical assays.

Next, we explored the underlying mechanism behind reduced microtubule binding affinity of methylated K317. From our simulations, it is evident that residue K317 associates with α-tubulin within a binding pocket formed by residues Q342, F343, D345 and T349. Therefore, we calculated the volume compatibility between K317 side chain and its binding pocket on the microtubule surface. The atomic volume of the nitrogen-bound hydrogen at the tip of K317 side chain, calculated by its van der Waals (VDW) radius defined in the simulations, perfectly fits in the α-tubulin binding pocket. Conversely, as hydrogen is replaced by the methyl group on K317, the side chain occupies a significantly larger space, resulting in steric clashes with binding pocket residues (Fig. 5C–D). In fact, methylated K317 can no longer bind to D345 and thus it is shifted upwards relative to the binding pocket, preferentially associating with D438 (Fig. 5E–F). Since the distance between residues K336 and D438 on α-tubulin is 4 Å larger than that between K336 and D345, residue K311 on Tau is pulled away from K336, eventually dissociating the Tau peptide from the tubulin-binding interface (Fig. 5F). We can conclude that the mechanism of action of K306/K317 methylation is multifaceted—it increases the lysine side chain steric hindrance and also alters the set of electrostatic interactions at the binding site.

4. Discussion

While the molecules and the cells involved in the initial inflammatory phase of MS have been unveiled to a large degree, much less is known about the molecular events underpinning the progressive course of the disease. Here, we demonstrate in the EAE model that the microtubule-associated protein Tau exerts a moderate, yet significant modifying activity on disease progression as Tau-deficient animals experience a more severe EAE

clinical manifestation in comparison to their wildtype littermates. Interestingly, Tau reduction in classic tauopathies can ameliorate, exacerbate or leave unaltered the pathologic phenotype, depending on the specific disease and animal model adopted [51, 52]. In the context of MS, while our observation is already present in the literature [13], we show for the first time that the beneficial effects of Tau on EAE phenotype are sex-specific. Other CNS signaling pathways have been reported to undergo sex-specific control in EAE [53] and strong gender effects have been described in the human disease as well. Specifically, while women are at increased risk of developing MS, men are more likely to display a progressive disease onset, poor recovery after initial attacks, and more rapid development of disability [54]. These differences are believed to be the result of complex interactions between genetic, epigenetic, and hormonal factors. It is also well established that AD and other dementias are more prevalent in women [55]. Also in AD models, Tau neurofibrillary pathology and cognitive impairment are more prominent in females than males [56, 57]. We present transcriptomic data suggesting the differential regulation between sexes of cytoskeletal dynamics in EAE pathology, which might explain, at least in part, the gender-specific effects of Tau. A number of microtubule-stabilizing proteins were found upregulated in wildtype males as compared to wildtype females in response to EAE, including the Tau-homolog microtubule-associated protein 2 (MAP2). We also identified neurotransmitter secretion as one of the Tau-related functions primarily affected in Tau-null male mice. Structural and functional synaptic alterations have been described in EAE models as well as in MS brain [58, 59], thus synaptic abnormalities are emerging as a critical pathogenic mechanism in MS [60]. Among the core genes driving the synaptic phenotype, α-synuclein encoding *Snca* resulted the most dysregulated one. Notably, also α-synuclein can bind tubulin and is known to physically interact with Tau in neurons [61, 62]. It has been recently discovered that α-synuclein itself is downregulated upon EAE and that *Snca*-knockout mice develop a more severe disease, somehow mirroring Tau-null animals [63]. It is thus conceivable that Tau and α-synuclein work synergistically as part of the same functional network to maintain cytoskeletal and synaptic stability against neuroinflammatory challenges.

The interactome analysis also highlighted that key components of the NF-κB activation machinery are upregulated upon EAE in the absence of Tau. Among them, RIPK3 is a hallmark mediator of necroptosis—a newly identified form of programmed necrosis occurring in inflammatory conditions [64]. In the context of neurodegeneration, necroptosis was shown to promote progressive axonal pathology and myelination defects [65]. Activated RIPK3 was also detected in MS lesions and necroptosis has been mechanistically connected to MS oligodendrocyte loss [66]. Hence, aberrant activation of this pathway might concur to the EAE phenotype and increased demyelination of Tau-deficient male mice.

Another key finding of our study is the down-regulation of Tau methylation at K306 in response to MOG-mediated CNS inflammation. It is well documented that PTMs dynamically modulate Tau subcellular localization and biochemical properties in response to intra- and extra-cellular stimuli [67]. However, lysine methylation of Tau is a relatively recent discovery and its impact on Tau biology as well as its significance in disease is still under debate. Disturbance of CNS methyl group metabolism has been connected with hyper-phosphorylated Tau accumulation upon neurodegeneration [68]. In the AD brain, misfolded Tau from neurofibrillary tangles was found mono-methylated at the level of 7 lysine residues

located in the projection and microtubule binding repeat regions [69]. For this reason, lysine methylation has been proposed to promote Tau aggregation by facilitating the interaction between molecules [70]. In contrast, there is *in vitro* evidence that methylated Tau display lower tendency toward aggregation and promotes microtubule assembly with the same efficiency of non-methylated Tau [71].

Here, we show that K306 methylation on Tau reduces its affinity for microtubules. By employing *in silico* and *in vitro* methods, we demonstrate that K306 directly interacts with the α-tubulin binding pocket and the methylation of its side chain lowers the binding strength due to a combination of steric hindrance effects and electrostatic interaction changes. To our knowledge, this is first study reporting the detailed molecular mechanism of how methylation of Tau affects the dynamics of its association with microtubules. Our observation of higher methylation in the mock (adjuvant and pertussis toxin)-injected animals appears counter-intuitive, but we speculate that the decrease in methylated K306 Tau levels in EAE might represent an adaptive mechanism aimed at preserving axonal integrity against neurotoxic insults (Fig. S4). In fact, encephalitogenic T cells are able to disrupt the neuronal microtubule network at the onset of EAE neurological deficits [72]. The evidence that a higher proportion of Tau-null mice reached EAE terminal stages is in agreement with this model (44% knockout mice vs 14% wildtype mice). Also the transcriptomic profiling confirms that more extended axonal dysfunctions take place upon EAE in the absence of Tau. Altogether, these findings suggest that Tau likely plays a role in the homeostatic response of neurons toward the inflammatory stress. In particular, in the context of CNS autoimmunity, the negative modulation of K306 methylation may facilitate the recovery from acute neuroinflammation and mediate the transition to the chronic stages of the disease. It is intriguing that we did not detect the same Tau PTM in female mice undergoing either acute or chronic EAE—this could possibly explain the sex-specific effect we observed in knockout mice. The transcriptional profiling analysis has highlighted a number of genes encoding lysine-specific demethylases as *Kdm5c*, *Kdm5d* and *Kdm6a* that map to the sex chromosomes (Table S1). As they are differentially expressed between genders, these enzymes represent relevant candidates to explain the sex-specific Tau methylation patterns and are warrant further investigation to explore whether Tau is one of their physiological substrates.

Notably, the mutation of the corresponding lysine in human Tau to an asparagine (K317N) or to a methionine (K317M) has been respectively associated with globular glial tauopathy (GGT) and fronto-temporal dementia with parkinsonism (FTDP), further corroborating the importance of this residue for Tau function [73, 74]. Also the K317N mutation impairs Tau capacity to induce tubulin assembly–evidence that highlights the structural constraints to which this domain has been subjected along evolution. In this regard, it is interesting that we did not detect differential methylation at K306 in the cuprizone model. We hypothesize that the acute administration of neurotoxic compounds overrides all the possible cellular responses that have evolved to counteract neurodegenerative stimuli.

Previous studies attempted to decipher, at least in part, the PTM profile of Tau upon EAE. In particular, the hyper-phosphorylation of both soluble and insoluble Tau fractions was described in the chronic phase of EAE at the AD-relevant epitopes T170, S202/T205, T201/

S203, T220 and S385/S393 [16]. In contrast, we have not detected differential phosphorylation in our proteomic profiling, with the exception of the threonine residue T100 showing suggestive hypophosphorylation in EAE, and the serine residues S401 and S405 showing hyper-phosphorylation (all with nominal significance). Intriguingly, both residues undergo hyper-phosphorylation also in AD brain [75, 76]. One possible explanation for these discrepancies resides in the different mouse strains and antigens used to induce EAE. Tau hyper-phosphorylation was indeed detected in Biozzi ADH mice immunized with whole spinal cord homogenates, which exhibit a typical chronic relapsing EAE [77]. In support of this hypothesis, a recent study failed to measure differences in S202 phosphorylation of soluble Tau in MOG-immunized C57BL/6J mice at acute and chronic EAE stages [78]. Interestingly, also the therapeutic efficacy of amyloid hexapeptides on EAE is influenced by genetic background where the C57BL/6J strain is susceptible to the treatment while the C57BL/10SnJ strain is not [79]. Altogether, such differences might reflect the heterogeneity and variability in the clinical and pathological manifestations of MS.

5. Conclusions

This work demonstrates that Tau is at the intersection between neuroinflammatory and neurodegenerative processes, as part of an adaptive mechanism aimed at preserving axonal integrity against neurotoxic insults. Additional studies will be required to fully decode the complex profile of Tau PTMs in MS lesions and correlate their effects on Tau function with specific aspects of the MS neuropathology and phenotype. Identifying the enzymes controlling such PTMs might provide novel therapeutic targets and pave the way to innovative strategies for enhancing Tau neuroprotective function.

Supplementary Material

Refer to Web version on PubMed Central for supplementary material.

Acknowledgements

AD and CC hold a Marilyn Hilton Award for Innovation in MS Research from the Conrad N. Hilton Foundation (#17323). The work was also supported by FISM-Fondazione Italiana Sclerosi Multipla Senior Research Fellowships Cod. 2014/B/1 and Cod. 2017/B/3 to AD and financed or co-financed with the "5 per mille" public funding, and the National Institutes of Health to JRO (R01NS026799) and to STW (R01NS081141). This work used the Extreme Science and Engineering Discovery Environment (XSEDE), which is supported by National Science Foundation grant number ACI-15485 under allocation MCB100146 (to MRK). The authors acknowledge the Nikon Imaging Center at UCSF and the Vincent Coates Foundation Mass Spectrometry Laboratory at Stanford University. The authors also thank Dr. Li Gan (Gladstone Institute, San Francisco, CA, USA) for providing the human Tau 2N4R construct, and Dr. Dejaegere and Dr. Grauffel (Université Louis Pasteur, Strasbourg, France) for sharing the methylated lysine force-field parameters.

Abbreviations

AD	Alzheimer’s disease
CC	corpus callosum
CHX	cycloheximide
CNS	central nervous system

CFA	complete Freund's adjuvant
DEG	differentially expressed gene
EAE	experimental autoimmune encephalomyelitis
FTD	fronto-temporal dementia
FTDP	fronto-temporal dementia with parkinsonism
GGT	globular glial tauopathy
GO	gene ontology
H&E	hematoxylin and eosin
HPRD	Human Protein Reference Database
LFB	luxol fast blue
MAP	microtubule-associated protein
MD	molecular dynamics
MS	multiple sclerosis
PTM	post-translational modification
PSP	progressive supranuclear palsy
VDW	van der Waals
VMD	Visual Molecular Dynamics

References

[1]. Wang Y, Mandelkow E Tau in physiology and pathology. Nat Rev Neurosci, 2016;17:5–21. [PubMed: 26631930]

[2]. Hong XP, Peng CX, Wei W, Tian Q, Liu YH, Yao XQ et al. Essential role of tau phosphorylation in adult hippocampal neurogenesis. Hippocampus, 2010;20:1339–49. [PubMed: 19816983]

[3]. Ahmed T, Van der Jeugd A, Blum D, Galas MC, D'Hooge R, Buee L et al. Cognition and hippocampal synaptic plasticity in mice with a homozygous tau deletion. Neurobiol Aging, 2014;35:2474–8. [PubMed: 24913895]

[4]. Lei P, Ayton S, Finkelstein DI, Spoerri L, Ciccotosto GD, Wright DK et al. Tau deficiency induces parkinsonism with dementia by impairing APP-mediated iron export. Nat Med, 2012;18:291–5. [PubMed: 22286308]

[5]. Kovacs GG Invited review: Neuropathology of tauopathies: principles and practice. Neuropathol Appl Neurobiol, 2015;41:3–23. [PubMed: 25495175]

[6]. Frank-Cannon TC, Alto LT, McAlpine FE, Tansey MG Does neuroinflammation fan the flame in neurodegenerative diseases? Mol Neurodegener, 2009;4:47. [PubMed: 19917131]

[7]. Glass CK, Saijo K, Winner B, Marchetto MC, Gage FH Mechanisms underlying inflammation in neurodegeneration. Cell, 2010;140:918–34. [PubMed: 20303880]

[8]. International Multiple Sclerosis Genetics Consortium, Patsopoulos NA, Baranzini SE, Santaniello A, Shoostari P, Cotsapas C, et al. The Multiple Sclerosis Genomic Map: Role of peripheral immune cells and resident microglia in susceptibility. bioRxiv, 2017.

[9]. Kutzelnigg A, Lucchinetti CF, Stadelmann C, Bruck W, Rauschka H, Bergmann M et al. Cortical demyelination and diffuse white matter injury in multiple sclerosis. Brain, 2005;128:2705–12. [PubMed: 16230320]

[10]. Frischer JM, Bramow S, Dal-Bianco A, Lucchinetti CF, Rauschka H, Schmidbauer M et al. The relation between inflammation and neurodegeneration in multiple sclerosis brains. Brain, 2009;132:1175–89. [PubMed: 19339255]

[11]. Yshii L, Gebauer C, Bernard-Valnet R, Liblau R Neurons and T cells: Understanding this interaction for inflammatory neurological diseases. Eur J Immunol, 2015;45:2712–20. [PubMed: 26345279]

[12]. Dendrou CA, Fugger L, Friese MA Immunopathology of multiple sclerosis. Nat Rev Immunol, 2015;15:545–58. [PubMed: 26250739]

[13]. Weinger JG, Davies P, Acker CM, Brosnan CF, Tsiperson V, Bayewitz A et al. Mice devoid of Tau have increased susceptibility to neuronal damage in myelin oligodendrocyte glycoprotein-induced experimental autoimmune encephalomyelitis. J Neuropathol Exp Neurol, 2012;71:422–33. [PubMed: 22487860]

[14]. Kurnellas MP, Adams CM, Sobel RA, Steinman L, Rothbard JB Amyloid fibrils composed of hexameric peptides attenuate neuroinflammation. Sci Transl Med, 2013;5:179ra42.

[15]. Kurnellas MP, Ghosn EE, Schartner JM, Baker J, Rothbard JJ, Negrin RS et al. Amyloid fibrils activate B-1a lymphocytes to ameliorate inflammatory brain disease. Proc Natl Acad Sci U S A, 2015;112:15016–23. [PubMed: 26621719]

[16]. Anderson JM, Hampton DW, Patani R, Pryce G, Crowther RA, Reynolds R et al. Abnormally phosphorylated tau is associated with neuronal and axonal loss in experimental autoimmune encephalomyelitis and multiple sclerosis. Brain, 2008;131:1736–48. [PubMed: 18567922]

[17]. Anderson JM, Patani R, Reynolds R, Nicholas R, Compston A, Spillantini MG et al. Evidence for abnormal tau phosphorylation in early aggressive multiple sclerosis. Acta Neuropathol, 2009;117:583–9. [PubMed: 19288121]

[18]. Didonna A, Benetti F Post-translational modifications in neurodegeneration. AIMS Biophysics, 2016;3:27–49.

[19]. Dawson HN, Ferreira A, Eyster MV, Ghoshal N, Binder LI, Vitek MP Inhibition of neuronal maturation in primary hippocampal neurons from tau deficient mice. J Cell Sci, 2001;114:1179–87. [PubMed: 11228161]

[20]. Didonna A, Cekanaviciute E, Oksenberg JR, Baranzini SE Immune cell-specific transcriptional profiling highlights distinct molecular pathways controlled by Tob1 upon experimental autoimmune encephalomyelitis. Sci Rep, 2016;6:31603. [PubMed: 27546286]

[21]. Zhang L, Yu W, Schroedter I, Kong J, Vrontakis M Galanin transgenic mice with elevated circulating galanin levels alleviate demyelination in a cuprizone-induced MS mouse model. PLoS One, 2012;7:e33901. [PubMed: 22442732]

[22]. Elias JE, Gygi SP Target-decoy search strategy for increased confidence in large-scale protein identifications by mass spectrometry. Nat Methods, 2007;4:207–14. [PubMed: 17327847]

[23]. Dobin A, Davis CA, Schlesinger F, Drenkow J, Zaleski C, Jha S et al. STAR: ultrafast universal RNA-seq aligner. Bioinformatics, 2013;29:15–21. [PubMed: 23104886]

[24]. Canto E, Isobe N, Didonna A, Group M-ES, Hauser SL, Oksenberg JR Aberrant STAT phosphorylation signaling in peripheral blood mononuclear cells from multiple sclerosis patients. J Neuroinflammation, 2018;15:72. [PubMed: 29514694]

[25]. Rodriguez-Martin T, Cuchillo-Ibanez I, Noble W, Nyenya F, Anderton BH, Hanger DP Tau phosphorylation affects its axonal transport and degradation. Neurobiol Aging, 2013;34:2146–57. [PubMed: 23601672]

[26]. Fitzpatrick AWP, Falcon B, He S, Murzin AG, Murshudov G, Garringer HJ et al. Cryo-EM structures of tau filaments from Alzheimer's disease. Nature, 2017;547:185–90. [PubMed: 28678775]

[27]. Waight AB, Bargsten K, Doronina S, Steinmetz MO, Sussman D, Prota AE Structural Basis of Microtubule Destabilization by Potent Auristatin Anti-Mitotics. PLoS One, 2016;11:e0160890. [PubMed: 27518442]

[28]. Kadavath H, Hofele RV, Biernat J, Kumar S, Tepper K, Urlaub H et al. Tau stabilizes microtubules by binding at the interface between tubulin heterodimers. Proc Natl Acad Sci U S A, 2015;112:7501–6. [PubMed: 26034266]

[29]. Humphrey W, Dalke A, Schulten K VMD: visual molecular dynamics. J Mol Graph, 1996;14:33–8, 27–8. [PubMed: 8744570]

[30]. Grauffel C, Stote RH, Dejaegere A Force field parameters for the simulation of modified histone tails. J Comput Chem, 2010;31:2434–51. [PubMed: 20652987]

[31]. Phillips JC, Braun R, Wang W, Gumbart J, Tajkhorshid E, Villa E et al. Scalable molecular dynamics with NAMD. J Comput Chem, 2005;26:1781–802. [PubMed: 16222654]

[32]. Huang J, Rauscher S, Nawrocki G, Ran T, Feig M, de Groot BL et al. CHARMM36m: an improved force field for folded and intrinsically disordered proteins. Nat Methods, 2017;14:71–3. [PubMed: 27819658]

[33]. Nosé S A molecular dynamics method for simulations in the canonical ensemble. Molecular Physics, 1984;52:255–68.

[34]. Durrant JD, Votapka L, Sorensen J, Amaro RE POVME 2.0: An Enhanced Tool for Determining Pocket Shape and Volume Characteristics. J Chem Theory Comput, 2014;10:5047–56. [PubMed: 25400521]

[35]. Towns J, Cockerill T, Dahan M, Foster I, Gaither K, Grimshaw A et al. XSEDE: Accelerating Scientific Discovery. Computing in Science & Engineering, 2014;16:62–74.

[36]. Prasad TS, Kandasamy K, Pandey A Human Protein Reference Database and Human Proteinpedia as discovery tools for systems biology. Methods Mol Biol, 2009;577:67–79. [PubMed: 19718509]

[37]. Cline MS, Smoot M, Cerami E, Kuchinsky A, Landys N, Workman C et al. Integration of biological networks and gene expression data using Cytoscape. Nat Protoc, 2007;2:2366–82. [PubMed: 17947979]

[38]. Ashburner M, Ball CA, Blake JA, Botstein D, Butler H, Cherry JM et al. Gene ontology: tool for the unification of biology. The Gene Ontology Consortium. Nat Genet, 2000;25:25–9. [PubMed: 10802651]

[39]. Zamvil SS, Steinman L Diverse targets for intervention during inflammatory and neurodegenerative phases of multiple sclerosis. Neuron, 2003;38:685–8. [PubMed: 12797954]

[40]. Huseby ES, Liggitt D, Brabb T, Schnabel B, Ohlen C, Goverman J A pathogenic role for myelin-specific CD8(+) T cells in a model for multiple sclerosis. J Exp Med, 2001;194:669–76. [PubMed: 11535634]

[41]. Herz J, Zipp F, Siffrin V Neurodegeneration in autoimmune CNS inflammation. Exp Neurol, 2010;225:9–17. [PubMed: 19961850]

[42]. Lei P, Ayton S, Moon S, Zhang Q, Volitakis I, Finkelstein DI et al. Motor and cognitive deficits in aged tau knockout mice in two background strains. Mol Neurodegener, 2014;9:29. [PubMed: 25124182]

[43]. Heinemann C, Heink S, Petermann F, Vasanthakumar A, Rothhammer V, Doorduijn E et al. IL-27 and IL-12 oppose pro-inflammatory IL-23 in CD4+ T cells by inducing Blimp1. Nat Commun, 2014;5:3770. [PubMed: 24796719]

[44]. LoPresti P, Szuchet S, Papasozomenos SC, Zinkowski RP, Binder LI Functional implications for the microtubule-associated protein tau: localization in oligodendrocytes. Proc Natl Acad Sci U S A, 1995;92:10369–73. [PubMed: 7479786]

[45]. Papadopoulos D, Pham-Dinh D, Reynolds R Axon loss is responsible for chronic neurological deficit following inflammatory demyelination in the rat. Exp Neurol, 2006;197:373–85. [PubMed: 16337942]

[46]. Matsushima GK, Morell P The neurotoxicant, cuprizone, as a model to study demyelination and remyelination in the central nervous system. Brain Pathol, 2001;11:107–16. [PubMed: 11145196]

[47]. Chung HH, Sze SK, Woo AR, Sun Y, Sim KH, Dong XM et al. Lysine methylation of progesterone receptor at activation function 1 regulates both ligand-independent activity and ligand sensitivity of the receptor. J Biol Chem, 2014;289:5704–22. [PubMed: 24415758]

[48]. Huq MD, Tsai NP, Khan SA, Wei LN Lysine trimethylation of retinoic acid receptor-alpha: a novel means to regulate receptor function. Mol Cell Proteomics, 2007;6:677–88. [PubMed: 17205979]

[49]. Morris M, Knudsen GM, Maeda S, Trinidad JC, Ioanoviciu A, Burlingame AL et al. Tau post-translational modifications in wild-type and human amyloid precursor protein transgenic mice. Nat Neurosci, 2015;18:1183–9. [PubMed: 26192747]

[50]. Lewis SA, Ivanov IE, Lee GH, Cowan NJ Organization of microtubules in dendrites and axons is determined by a short hydrophobic zipper in microtubule-associated proteins MAP2 and tau. Nature, 1989;342:498–505. [PubMed: 2511449]

[51]. Vossel KA, Zhang K, Brodbeck J, Daub AC, Sharma P, Finkbeiner S et al. Tau reduction prevents Abeta-induced defects in axonal transport. Science, 2010;330:198. [PubMed: 20829454]

[52]. Morris M, Koyama A, Masliah E, Mucke L Tau reduction does not prevent motor deficits in two mouse models of Parkinson's disease. PLoS One, 2011;6:e29257. [PubMed: 22206005]

[53]. Krementsov DN, Noubade R, Dragon JA, Otsu K, Rincon M, Teuscher C Sex-specific control of central nervous system autoimmunity by p38 mitogen-activated protein kinase signaling in myeloid cells. Ann Neurol, 2014;75:50–66. [PubMed: 24027119]

[54]. Bove R, Chitnis T Sexual disparities in the incidence and course of MS. Clin Immunol, 2013;149:201–10. [PubMed: 23608496]

[55]. Lewis J, Dickson DW, Lin WL, Chisholm L, Corral A, Jones G et al. Enhanced neurofibrillary degeneration in transgenic mice expressing mutant tau and APP. Science, 2001;293:1487–91. [PubMed: 11520987]

[56]. Yue M, Hanna A, Wilson J, Roder H, Janus C Sex difference in pathology and memory decline in rTg4510 mouse model of tauopathy. Neurobiol Aging, 2011;32:590–603. [PubMed: 19427061]

[57]. Mazure CM, Swendsen J Sex differences in Alzheimer's disease and other dementias. Lancet Neurol, 2016;15:451–2. [PubMed: 26987699]

[58]. Dutta R, Chang A, Doud MK, Kidd GJ, Ribaudo MV, Young EA et al. Demyelination causes synaptic alterations in hippocampi from multiple sclerosis patients. Ann Neurol, 2011;69:445–54. [PubMed: 21446020]

[59]. Zhu B, Luo L, Moore GR, Paty DW, Cynader MS Dendritic and synaptic pathology in experimental autoimmune encephalomyelitis. Am J Pathol, 2003;162:1639–50. [PubMed: 12707048]

[60]. Mandolesi G, Gentile A, Musella A, Fresegna D, De Vito F, Bullitta S et al. Synaptopathy connects inflammation and neurodegeneration in multiple sclerosis. Nat Rev Neurol, 2015;11:711–24. [PubMed: 26585978]

[61]. Cartelli D, Aliverti A, Barbiroli A, Santambrogio C, Ragg EM, Casagrande FV et al. alpha-Synuclein is a Novel Microtubule Dynamase. Sci Rep, 2016;6:33289. [PubMed: 27628239]

[62]. Jensen PH, Hager H, Nielsen MS, Hojrup P, Gliemann J, Jakes R alpha-synuclein binds to Tau and stimulates the protein kinase A-catalyzed tau phosphorylation of serine residues 262 and 356. J Biol Chem, 1999;274:25481–9. [PubMed: 10464279]

[63]. Ettle B, Kuhbandner K, Jorg S, Hoffmann A, Winkler J, Linker RA Alpha-Synuclein deficiency promotes neuroinflammation by increasing Th1 cell-mediated immune responses. J Neuroinflammation, 2016;13:201. [PubMed: 27565429]

[64]. Shlomovitz I, Zargrian S, Gerlic M Mechanisms of RIPK3-induced inflammation. -Immunol Cell Biol, 2017;95:166–72. [PubMed: 27974745]

[65]. Ito Y, Ofengeim D, Najafov A, Das S, Saberi S, Li Y et al. RIPK1 mediates axonal degeneration by promoting inflammation and necroptosis in ALS. Science, 2016;353:603–8. [PubMed: 27493188]

[66]. Ofengeim D, Ito Y, Najafov A, Zhang Y, Shan B, DeWitt JP et al. Activation of necroptosis in multiple sclerosis. Cell Rep, 2015;10:1836–49. [PubMed: 25801023]

[67]. Haj-Yahya M, Lashuel HA Protein Semisynthesis Provides Access to Tau Disease-Associated Post-translational Modifications (PTMs) and Paves the Way to Deciphering the Tau PTM Code in Health and Diseased States. J Am Chem Soc, 2018;140:6611–21. [PubMed: 29684271]

[68]. Obeid R, Kasoha M, Knapp JP, Kostopoulos P, Becker G, Fassbender K et al. Folate and methylation status in relation to phosphorylated tau protein(181P) and beta-amyloid(1–42) in cerebrospinal fluid. Clin Chem, 2007;53:1129–36. [PubMed: 17384003]

[69]. Thomas SN, Funk KE, Wan Y, Liao Z, Davies P, Kuret J et al. Dual modification of Alzheimer's disease PHF-tau protein by lysine methylation and ubiquitylation: a mass spectrometry approach. Acta Neuropathol, 2012;123:105–17. [PubMed: 22033876]

[70]. Sinha S, Lopes DH, Du Z, Pang ES, Shanmugam A, Lomakin A et al. Lysine-specific molecular tweezers are broad-spectrum inhibitors of assembly and toxicity of amyloid proteins. J Am Chem Soc, 2011;133:16958–69. [PubMed: 21916458]

[71]. Funk KE, Thomas SN, Schafer KN, Cooper GL, Liao Z, Clark DJ et al. Lysine methylation is an endogenous post-translational modification of tau protein in human brain and a modulator of aggregation propensity. Biochem J, 2014;462:77–88. [PubMed: 24869773]

[72]. Shriver LP, Dittel BN T-cell-mediated disruption of the neuronal microtubule network: correlation with early reversible axonal dysfunction in acute experimental autoimmune encephalomyelitis. Am J Pathol, 2006;169:999–1011. [PubMed: 16936273]

[73]. Tacik P, DeTure M, Lin WL, Sanchez Contreras M, Wojtas A, Hinkle KM et al. A novel tau mutation, p.K317N, causes globular glial tauopathy. Acta Neuropathol, 2015;130:199–214. [PubMed: 25900293]

[74]. Zarranz JJ, Ferrer I, Lezcano E, Forcadas MI, Eizaguirre B, Atares B et al. A novel mutation (K317M) in the MAPT gene causes FTDP and motor neuron disease. Neurology, 2005;64:1578–85. [PubMed: 15883319]

[75]. Yamamoto H, Hiragami Y, Murayama M, Ishizuka K, Kawahara M, Takashima A Phosphorylation of tau at serine 416 by Ca2+/calmodulin-dependent protein kinase II in neuronal soma in brain. J Neurochem, 2005;94:1438–47. [PubMed: 16000144]

[76]. Hanger DP, Byers HL, Wray S, Leung KY, Saxton MJ, Seereeram A et al. Novel phosphorylation sites in tau from Alzheimer brain support a role for casein kinase 1 in disease pathogenesis. J Biol Chem, 2007;282:23645–54. [PubMed: 17562708]

[77]. Baker D, O'Neill JK, Gschmeissner SE, Wilcox CE, Butter C, Turk JL Induction of chronic relapsing experimental allergic encephalomyelitis in Biozzi mice. Journal of Neuroimmunology, 1990;28:261–70. [PubMed: 2373763]

[78]. Frid K, Einstein O, Friedman-Levi Y, Binyamin O, Ben-Hur T, Gabizon R Aggregation of MBP in chronic demyelination. Ann Clin Transl Neurol, 2015;2:711–21. [PubMed: 26273684]

[79]. Kraus A, Race B, Phillips K, Winkler C, Saturday G, Kurnellas M et al. Genetic background modulates outcome of therapeutic amyloid peptides in treatment of neuroinflammation. J Neuroimmunol, 2016;298:42–50. [PubMed: 27609274]

Highlights

- Tau exerts a sex-specific protective effects on disease progression in EAE
- Lower levels of Tau methylation at lysine K306 are found in mice at chronic EAE stages
- Methylation at K306 modulates Tau affinity for microtubules
- Downregulation of K306 methylation might represent a homeostatic response to increase axonal stability

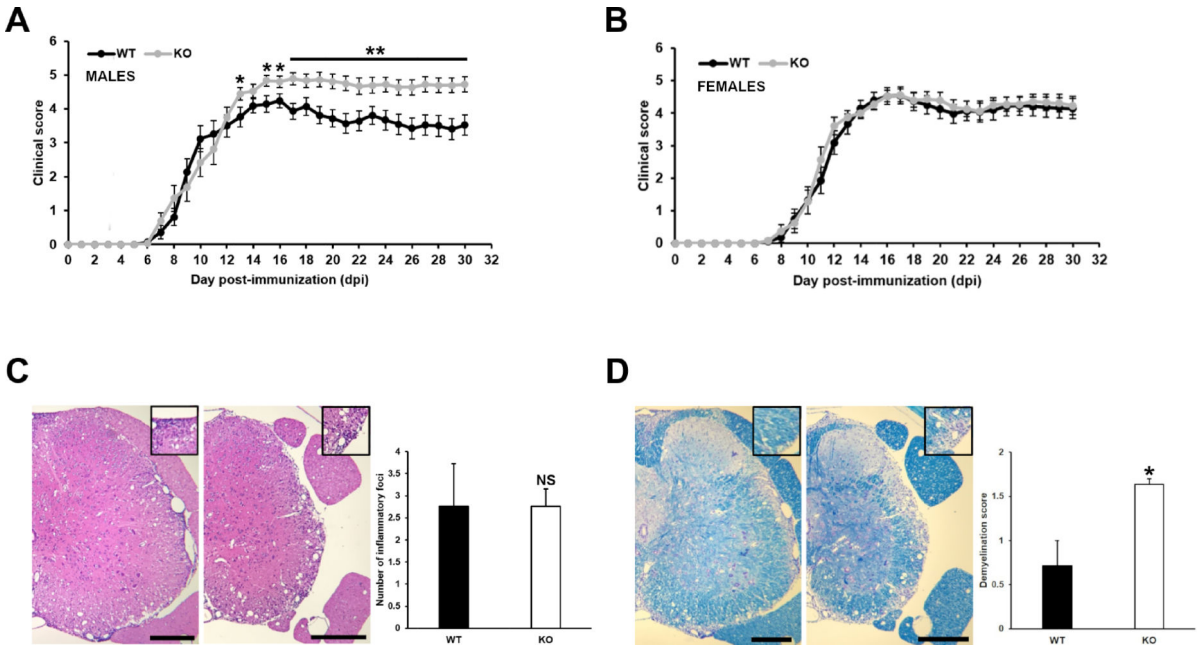

Figure 1. Tau-null male mice experience a more severe EAE clinical course.

(A-B) *Mapt*$^{-/-}$ and wildtype littermates (*Mapt*$^{+/+}$) either males or females were immunized with $MOG_{35–55}$ peptide as detailed in the Material and Methods section and scored daily up to 30 days post-injection. Mean scores ±SEM from two independent experiments are plotted (WT males =21; KO males=18; WT females=22; KO females=20). *P≤0.05, **P≤0.01; Mann-Whitney U test. (C-D) Histopathological analysis of representative spinal cords from male EAE mice at 31 dpi (N=3 per genotype) using hematoxylin and eosin or luxol fast blue. The top right images in C and D depict respectively typical inflammatory foci (groups of >20 infiltrating cells) and demyelinated lesions at high magnification. The quantification plots for cellular infiltration (mean number of inflammatory foci ±SEM) and myelin loss (mean demyelination score ±SEM) are also shown in each panel. Scale bar: 200 μm. *P≤0.05; two tailed student's t-test. NS; non-significant.

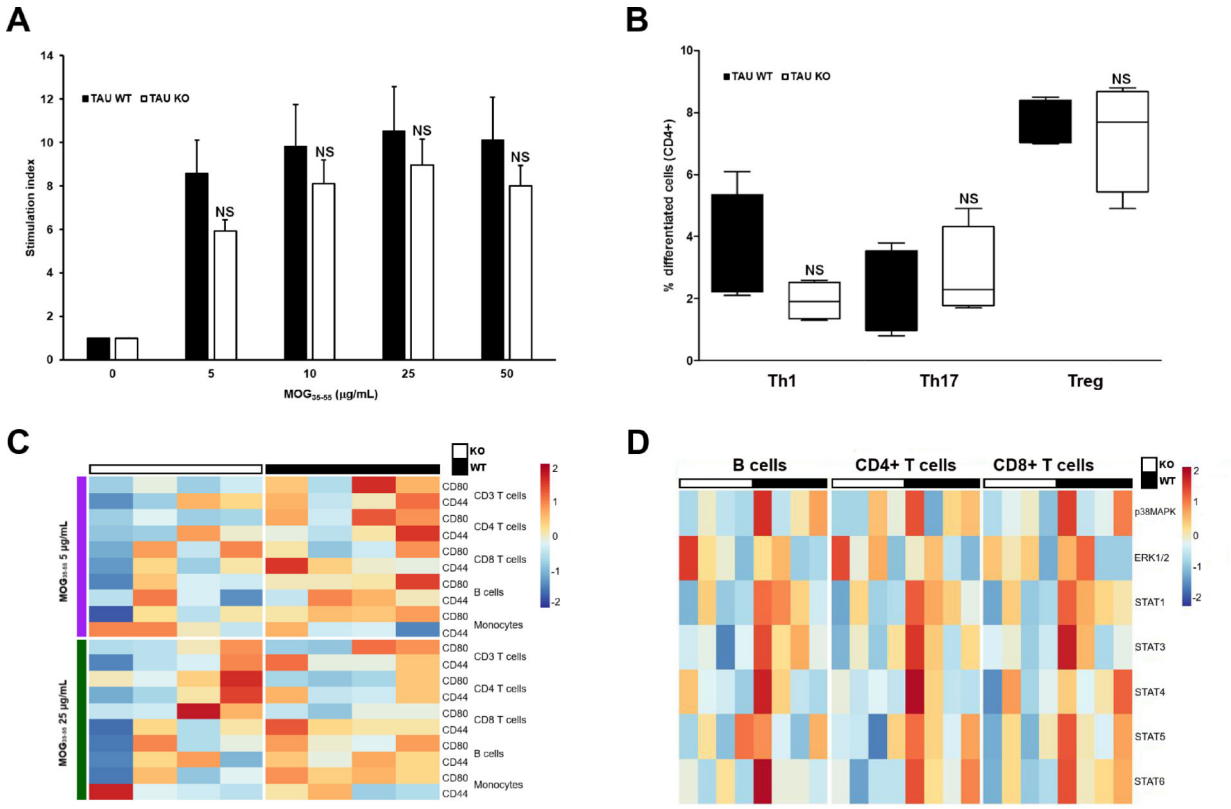

Figure 2. Tau deficiency does not affect the autoimmune response.

(A) Splenocytes from *Mapt*$^{-/-}$ and wildtype male mice primed with $MOG_{35–55}$ peptide for 11 days were re-stimulated *in vitro* with increasing concentrations of $MOG_{35–55}$ peptide and their proliferation was assessed after 3 days by thymidine incorporation. The differences are expressed as fold-increases to the proliferation rate of non-stimulated cells. (B) Splenocytes from *Mapt*$^{-/-}$ and wildtype male mice primed with MOG peptide were re-stimulated *in vitro* with 10 µg/mL $MOG_{35–55}$ peptide in polarizing conditions toward Th1, Th17 and Treg lineages. After 3 days, the percentage of $CD4^+$ T cells acquiring the different phenotypes was assessed by flow cytometry via intracellular cytokine staining (for Th1/Th17) or FOXP3 staining (for Treg). (C) Splenocytes from MOG peptide-primed *Mapt*$^{-/-}$ and wildtype male mice were re-stimulated with 5 or 25 µg/mL $MOG_{35–55}$ peptide for 3 days and the surface expression of the activation markers CD44 and CD80 was measured by flow cytometry in $CD3^+$, $CD4^+$ and $CD8^+$ T cells, B cells and monocytes. (D) Splenocytes from MOG peptide-primed *Mapt*$^{-/-}$ and wildtype male mice were re-stimulated with 10 µg/mL $MOG_{35–55}$ peptide for 24 hours and the activation status of 7 phosphoproteins (p38, ERK1/2, STAT1, STAT3–6) was assessed by phosphoflow cytometry in $CD4^+$ and $CD8^+$ T cells, and in B cells. For panels C and D, the fluorescence values were converted in Z-scores and plotted as heatmaps where each column represents a different mouse and each row depicts the levels of a surface marker or a phosphoprotein in a specific cell population. 4 mice per genotype were used in the different analyses. NS; non-significant.

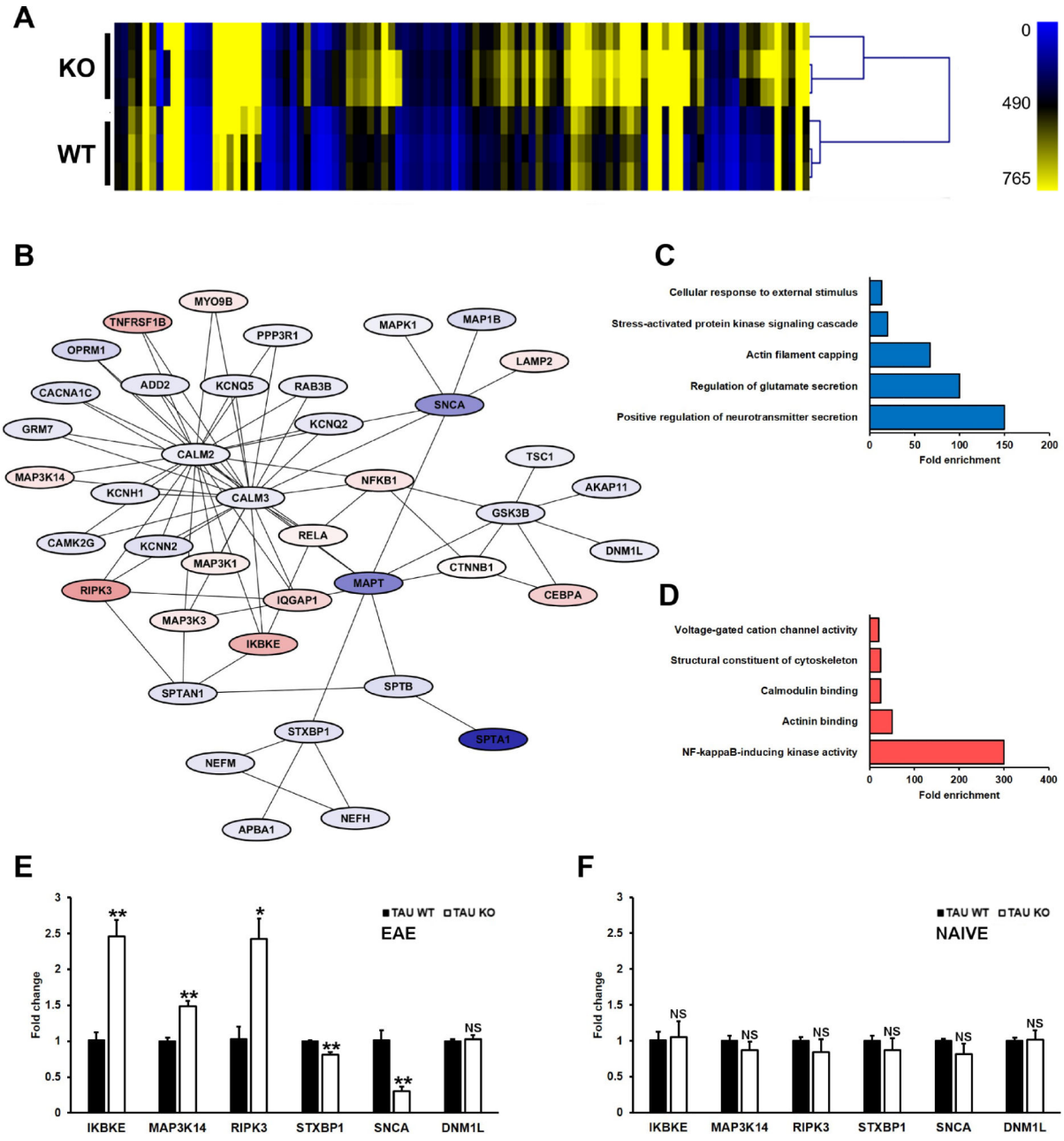

Figure 3. Transcriptomic analysis of Tau-null mice upon EAE induction.

(A) Unsupervised hierarchical clustering of FPKM values for the genes with the highest variance (SD>50) that are expressed in spinal cords from Tau-null and wildtype male mice (N=3 per genotype) at 33 dpi of EAE. The distances between genes or samples were calculated using Spearman correlation. (B) Gene network of Tau interacting proteins in EAE spinal cord obtained by superimposing the differentially expressed genes from WT-KO comparison (adjusted P<0.05) onto the Tau protein interaction network accessible at the Human Protein Reference Database (HPRD). Nodes in red correspond to genes overexpressed in knockout mice as compared to wildtype controls while nodes in blue indicate underexpressed genes. (C-D) Histograms showing the top 5 most enriched gene

ontology (GO) terms among the significant ones (adjusted P<0.05) in the molecular function and biological process categories. GO analysis was conducted on the genes within the Tau network. (E) Validation of RNA-seq results by qRT-PCR on selected genes from each GO category. (F) The same genes were also tested for expression in the spinal cord of naïve mice (N=3 per genotype). Expression levels are shown as fold differences (mean ±SEM) compared to wildtype mice. *P≤0.05, **P≤0.01; two tailed student's t-test. NS; non-significant.

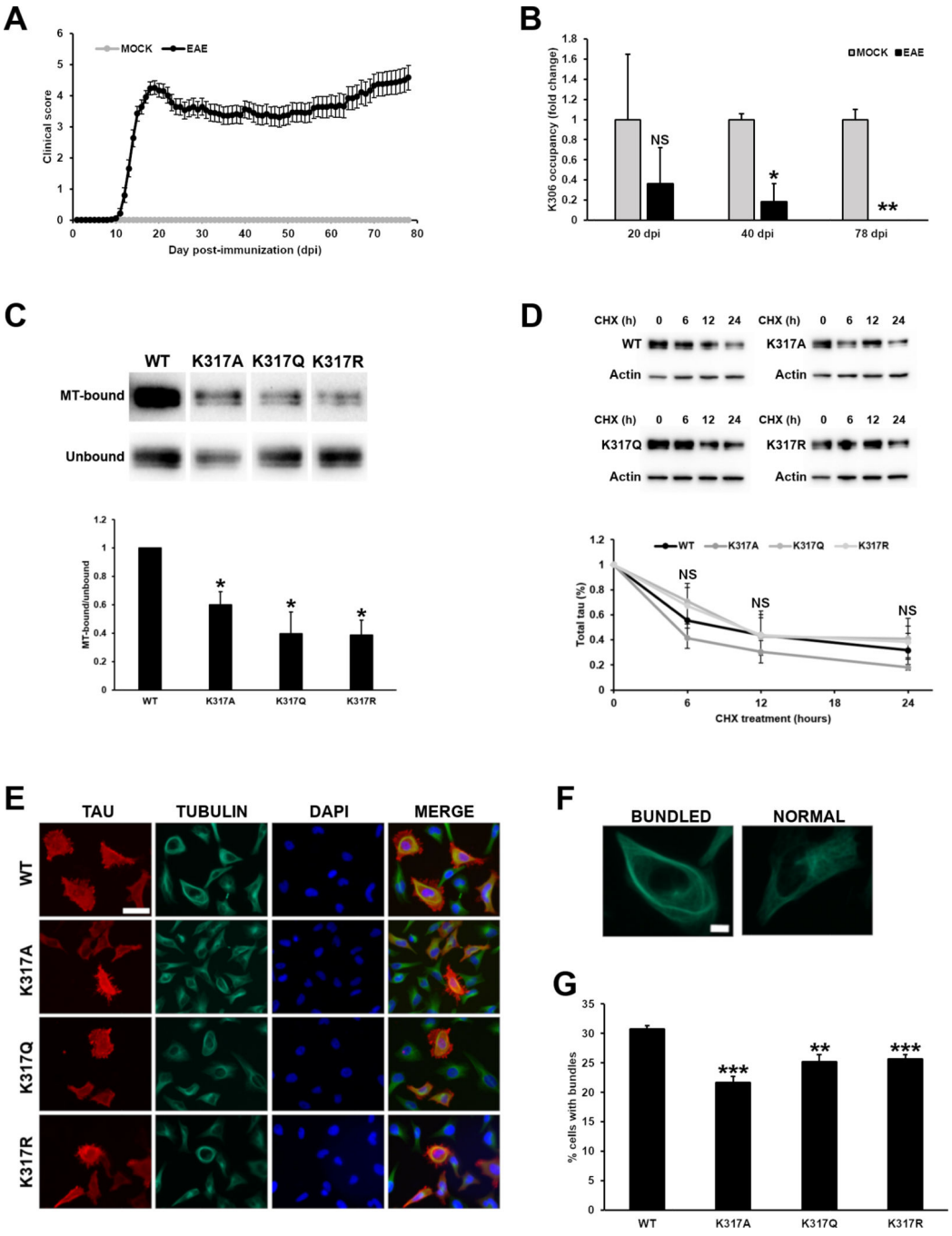

Figure 4. Proteomic analysis of Tau PTMs in EAE mice.

(A) EAE was inducted in C57BL/6J male mice and spinal cords were collected from 3 mice at baseline, at the peak of disease (20 dpi; EAE score=5), after recovery (40 dpi; EAE score=4) and at chronic stages (78 dpi; EAE score=4). Spinal cords from 3 mock injected mice were also collected at the same time points as controls. Tau was immunoprecipitated from spinal cord tissues and subjected to proteomic PTM profiling. (B) Relative levels of methylation at K306 residue in Tau sequence for EAE and mock injected animals at different disease stages. (C) HeLa cells were transfected with expression vectors carrying a

FLAG-tagged wildtype Tau (N2R4) sequence or the mutants K317A, K317Q and K317R. After 24 hours, cell lysates were separated into microtubule-bound and unbound fractions and probed by Western blot for Tau levels using an anti-FLAG antibody. The bound/unbound ratios relative to wildtype Tau were plotted for each mutant. The results (mean ±SEM) derive from 3 independent experiments. (D) HeLa cells expressing wildtype Tau or the mutants K317A, K317Q and K317R were treated with cycloheximide (25 μg/mL) for 6h, 12h and 24h. Cell lysates collected at the different time points were then probed for Tau and actin by Western blot. Tau levels normalized to actin were plotted as percentage of the baseline levels. The results (mean ±SEM) derive from 3 independent experiments. (E) HeLa expressing wildtype Tau or the mutants K317A, K317Q and K317R were seeded on poly-L-lysine coated coverslips and fixed with 4% PFA. After permeabilization, cells were immunostained for Tau (in red) and tubulin (in green). Nuclei were counterstained with DAPI (in blue). Scale bar: 50 μm. (F) High magnification pictures of HeLa cells exhibit tubulin bundles or a normal tubulin network. Scale bar: 10 μm. (G) 5–6 random fields were imaged for each Tau construct and the number of transfected cells showing tubulin bundles was quantified. The results (mean ±SEM) derive from 3 independent experiments in which more than 2000 cells were analyzed for each construct. *P≤0.05, **P≤0.01, ***P≤0.005; two tailed student's t-test. NS; non-significant.

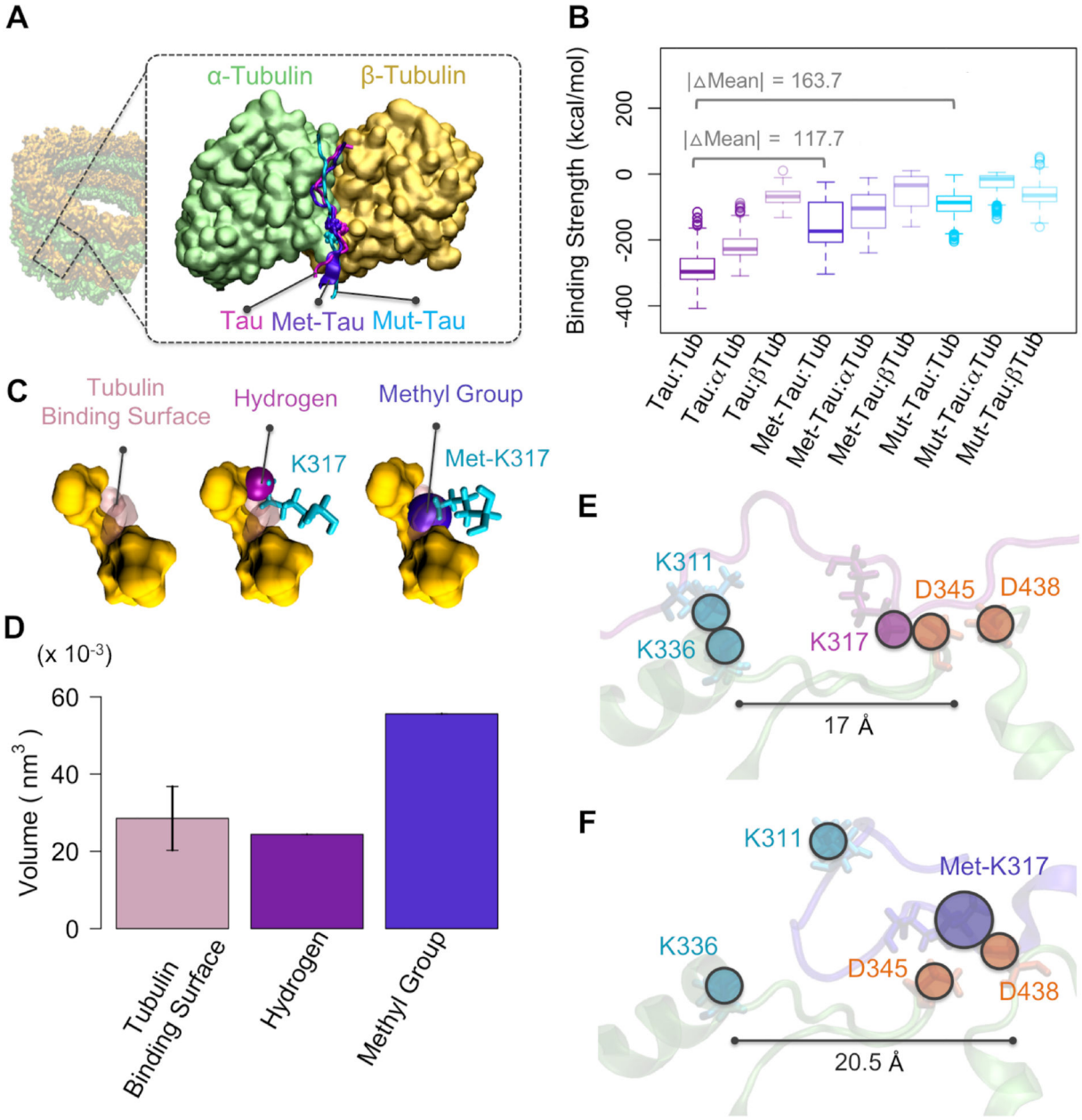

Figure 5. Molecular dynamics simulations of Tau-microtubule binding.

(A) The initial configurations of molecular simulations were constructed by positioning residues 311 of wildtype Tau (PDB ID: 5O3T) shown in *magenta* near residues 336 and 338 of α-tubulin (PDB ID: 5IYZ). Methylated Tau (*purple*) was positioned similar to the wildtype to facilitate comparison. (B) Boxplots depict distributions of the interaction energies of wildtype/methylated/mutated Tau with both α-β tubulin monomers and dimer. The interaction of wildtype Tau with tubulin dimer was significantly stronger than both methylated and mutated Tau molecules ($P< 2.2\times10^{-16}$). The absolute values of differences between the average interaction energies ($|\Delta Mean| = |Mean\ Energy_{\ Wildtype\ Tau:\ Microtubule} - Mean\ Energy_{\ Methylated/Mutated\ Tau:\ Microtubule}|$) are noted above brackets. (C) Visualizations of the binding pocket volume of K317 on the α-tubulin surface (*pink*), the VDW volume of

the K317 hydrogen atom (*magenta*), which is replaced upon methylation, and the VDW volume of the methyl group (*purple*). (D) The VDW volume of the K317 hydrogen atom matches the pocket volume, whereas the methyl group is significantly larger and does not fit into the binding pocket. Variation of the pocket volume indicated by standard deviation, results from fluctuations of the protein surface, however, the molecular volumes are fixed throughout the simulations. (E) The R3 repeat of wildtype Tau extends along residues K336 and D345 of α-tubulin. (F) Methylation of K317 inhibits its binding to D345 on α-tubulin due to the volume mismatch between methyl group and the binding pocket, and shifts it towards D438, which results in pulling K311 away from K336.